Enhancing the electrochemical performance of Boron Nitride@ Hematite/Graphene Oxide (BN@α-Fe_2O_3/GO) hybrid composites for next-generation supercapacitors

S. Shams [a, *], B. Bindhu [a]
[a] *Department of Physics, Noorul Islam Centre for Higher Education, Kumaracoil, Thuckalay, 629180, Tamil Nadu, India.*

Hybrid nanocomposites with enhanced electrochemical performance have drawn considerable interest in the area of high-performance energy storage systems. Here, we demonstrate the effective preparation of a multifunctional BN@α-Fe_2O_3/GO composite through a hydrothermal synthesis process, with the structural stability of boron nitride (BN), redox property of hematite (α-Fe_2O_3), and remarkable conductivity and surface area of graphene oxide (GO). The structural and morphological properties supported the successful integration and uniform distribution of the constituent materials, ensuring enhanced electrochemical behaviors. BN@α-Fe_2O_3/GO composite exhibits exceptional specific capacitance at varying current densities: 1001.2 F/g at 3Ag^{-1}, 971.5 F/g at 4 Ag^{-1}, 815.9 F/g at 5 Ag^{-1}, and 808.78 F/g at 7 $Ag^{-1,}$ respectively, highlighting its viability as a high-performing electrode component for electrochemical devices. Furthermore, this composite delivers excellent cyclic stability and rate capability, retaining 82.7% of its capacitance around 10000 cycles. The resultant BN@α-Fe_2O_3/GO composite displays a power density of 750W kg^{-1} with an energy density of 34.76Wh kg^{-1}. These remarkable findings reflect the superior charge storage efficiency and rapid energy delivery capability of the composite. The structural integrity of BN@α-Fe_2O_3/GO hybrid composites is because of the synergistic combination of BN, α-Fe_2O_3, and GO, thus promoting efficient ion transport and diffusion mechanisms. The exceptional electrochemical behavior exhibited by BN@α-Fe_2O_3/GO composites is a result of this combination, indicating its suitability as electrode materials for supercapacitor applications.

(Received: September 19, 2025, Accepted: December 8, 2025)

Keywords: Boron nitride (BN), Electrochemical, Energy storage, Graphene oxide (GO), Hematite(α-Fe_2O_3), Hydrothermal, Supercapacitor

1. Introduction

In recent decades, research on energy storage devices has garnered remarkable attention driven by the rising global energy requirements, thus focusing on its sustainability. Among the many devices for electrochemical energy storage systems, the supercapacitor has gained significant attention owing to its unique ability to overcome the performance gap that exists between conventional energy storage devices [1-3]. Supercapacitors possess excellent cycling capacity and stability, high power density, and also offer faster charge-discharge rates. Hence, supercapacitors are widely utilized in various applications, from powering hybrid electric vehicle (HEVs) and portable devices, industrial power control, to emergency backup power [4].

The search for high-performance supercapacitors relies heavily on the electrode materials, which strongly affect power density, operating voltage, cycling stability, coulombic efficiency, energy density, and specific capacitance. Because of these exceptional properties, a lot of research is ongoing on advanced materials, including graphene, graphene oxide, hexagonal boron nitride(h-BN), Molybdenum disulfide (MoS_2), transition metal oxides (TiO_2, Fe_2O_3, Fe_3O_4, V_2O_5, etc), etc [5]. Boron nitride (BN), a two-dimensional layered material, shows high stability (both thermal and

* Corresponding author: shamsiyashams64@gmail.com
https://doi.org/10.15251/JOR.2025.216.799

chemical), good mechanical stability, a wide band-gap, and unique surface properties [6]. Graphene oxide (GO), on the other hand, is a material derived from graphene, is electrically conductive with adjustable surface functionalities, facilitating faster ion transport [7]. On the other hand, hematite (α-Fe_2O_3), a low-cost, eco-friendly iron oxide with an average band gap of 2.1 to 2.4 eV, is widely used in various electrochemical energy storage applications [8]. To the best of our understanding, BN, when used independently as an electrode material, exhibits limited potential as a supercapacitor material, mainly associated to its strong interlayer van der Waals interactions, elevated surface energy, and wide band gap (5.4 to 6.04 eV) [9], limiting rapid ion-charge transfers, thus lowering the electrochemical capacitance. Such characteristics result in restricted electronic conductivity and considerable structural fluctuations during the charge-discharge cycles. However, the other individual materials face certain drawbacks: GO tends to stack and agglomerate, thus reducing the active surface area, and α-Fe_2O_3 undergoes structural degradation during repeated charge-discharge cycles.

Furthermore, studies proved that the rational design of composites that combines the benefits of the different components is a distinctly promising avenue to overcome the limitations of each material, resulting in electrodes that take advantage of conductivity and active surface area. This broad research effort has prioritized the synthesis of hybrid composite materials, aiming to tune materials with desirable properties. For instance, Bongu *et al*. [10] fabricated a hybrid h-BN/G/MOS_2 composite that demonstrated excellent electrochemical performance as an electrode material, achieving a specific capacitance of 392 F/g at 1 Ag^{-1} and retaining 96.4% of its capacity after 10,000 charge-discharge cycles. Similarly, Maity *et al*. [11] prepared Fe_2O_3/rGO composites via microwave microwave-assisted technique, displaying a specific capacitance of 136 C/g, a cyclic stability of about 83%, with an average energy density value of 10.5 Wh kg^{-1}. Shilpi *et al.* fabricated an interconnected hybrid structure comprising tungsten disulfide, reduced graphene oxide, and carbon nanotubes (WS_2/rGO/CNT) [12]. Astonishingly, this hybrid supercapacitor yields a volumetric capacitance of about 67.60 F/g and an exceptional power density of 115.01 W kg^{-1}, respectively.

The recent literature surveys indicate that the hybrid materials can overcome drawbacks faced by the individual materials, thus enhancing their characteristic features, enabling their usage in electrochemical systems. In the ongoing quest for advanced hybrid materials, our present research work focuses on the hydrothermal synthesis of Boron nitride-based graphene oxide/hematite (BN@α-Fe_2O_3/GO) composite as detailed in Fig. 4b. This study provided new insights into material design approaches, and to our knowledge, this composite has not been previously reported. The introduction of the GO function as a conductive scaffold that allows the passage of electrons as well as absorb mechanical strain, while the functional groups can provide anchor points for the Fe_2O_3 nanoparticles. The α-Fe_2O_3 component aids in energy storage by facilitating pseudo capacitance, which relies on reversible reduction-oxidation reactions [13]. BN used within the composite delivers thermal stability and mechanical reinforcement while inhibiting GO restacking by acting as a spacer between layers and maintaining a high energy accessible surface area. More recent studies have shown that exfoliated BN and functionalized-BN containing conductive species modestly increase the overall conductivity of the composite, particularly when dispersed into an electronically active matrix [14]. The hydrothermal synthesis approach offers a regulated and eco-friendly pathway to develop the BN@α-Fe_2O_3/GO composite with modified structural and electrochemical properties. It allows synergistic interactions between the component materials, eliminating their shortcomings while improving the overall behavior of the hybrid for supercapacitor applications. This technique facilitates the homogeneous dispersion of α-Fe_2O_3 nanoparticles across the surface of the GO along with the simultaneous incorporation of BN in the matrix, thus improving the specific capacitance and durability in terms of cycling stability. A series of structural, morphological, and electrochemical analyses of the as- prepared composites is conducted. The experimental data are rationally reported and discussed. In conclusion, this work constitutes a major advancement in the fabrication of functional nanomaterials specifically designed for next-generation supercapacitor systems.

2. Experimental section

2.1. Materials

Hexagonal boron nitride (h-BN, purity ≥ 99.8%), graphite powder (purity ≥ 99.8%), and iron oxide nanopowder (purity ≥ 99.5%) were obtained from Sigma-Aldrich (USA). Sodium hydroxide (NaOH) of purity between 95–99%, Phosphoric acid(H_3PO_4), hydrogen peroxide (H_2O_2), sulfuric acid (H_2SO_4), and hydrochloric acid (HCl) were also obtained from Sigma-Aldrich (USA). Potassium permanganate ($KMnO_4$) (purity ≥ 98%) was purchased from Loba Chemie Pvt. Ltd. (India). Reagents, including deionized (DI) water and dimethyl formamide (DMF) (sourced from Merck,India), were of analytical reagent (AR) grade and possessed high purity. These materials were used precisely as received, eliminating the need for additional purification steps.

2.2. Preparation of exfoliated BN

Exfoliated BN nanosheets are synthesized via liquid-phase exfoliation [15]. Initially, a bulk powder of BN with dimethylformamide (DMF) was stirred for about 45–50 minutes to facilitate a homogeneous dispersion. Then the supernatant mixture undergoes ultrasonication, which disrupts the weak van der Waals interlayer forces. To eliminate unexfoliated residues, the suspension underwent centrifugation at 4000rpm. The resulting supernatant, containing the exfoliated BN was collected. The collected BN was then subjected to heating at 80°C for about 46 hrs to effectively dry the sample.

2.3. Preparation of graphene oxide (GO)

Utilizing the modified Hummers method, as detailed in previous reports [16], graphite flakes served as the precursor material for the synthesis of GO. The standard experimental procedure is as follows: graphite flakes are dispersed in a mixed acid solution of sulphuric acid and phosphoric acid (3:1 ratio), mounted on an ice bath. This mixture undergoes constant stirring. After 20minutes, potassium permanganate is added dropwise to the above-mentioned mixture, maintaining the temperature and ensuring uniform oxidation. The reaction mixture is subjected to agitation for about 7h, until the solution gradually changes its colour to dark green, reflecting the oxidation of graphite. The mixture is treated using hydrogen peroxide, followed by the addition of deionized water, leading to a change of colour to yellowish brown, thus confirming the formation of oxidized graphene. The obtained dispersion is kept undisturbed for about 8–9 hr for the sedimentation process. The precipitate thus obtained is collected, undergoes a centrifugation process at 3500 rpm, followed by a thorough washing process using an HCl solution and subsequently DI water. The material was then dried in an oven for 24 hr, at a temperature of 90 ^{0}C to yield GO, powdered and kept in sealed containers.

2.4. Preparation of BN@α-Fe_2O_3/GO hybrid composites

Initially, α-Fe_2O_3 nanoparticles were suspended in distilled water and underwent intense magnetic stirring for about 30 minutes to ensure a homogenous suspension. The as-modified boron nitride (BN) is then added to this homogenous suspension and stirred for an additional 1 hour to promote blending between the components. To enhance the properties, a small amount of NaOH is added. This addition of NaOH improves the dispersibility, active surface sites, and also allows improved integration with other nanomaterials in the eventual formation of hybrid composites [17]. Following this, GO is added to the aforementioned suspension, and the mixture is further subjected to stirring to ensure homogeneity. To improve particle agglomeration and dispersion, the above mixture underwent microwave-assisted ultrasonication for about 1 hour. The process is optimized for localized heating, thereby improving the contact interface between BN, GO, and α-Fe_2O_3 constituents. The sonicated mixture is then placed inside a 150 mL Teflon-lined stainless-steel autoclave for the subsequent reaction inside an electric oven maintaining a temperature of about 120 ^{0}C for about 8 hr. High temperature and pressure environments within the autoclave favored the integration of well-formed hybrid composites exhibiting enhanced interfacial interactions among the constituents. After the hydrothermal synthesis, the reaction vessel underwent natural cooling to room temperature. This prepared hybrid BN@α-Fe_2O_3/GO composite material was centrifuged at 3500 rpm and harvested. The product was thoroughly washed with DI water and ethanol to remove excess reaction byproducts. Final drying was performed in an oven at 80 ^{0}C for a duration of 6 hrs. The yielded composite (BN@α-Fe_2O_3/GO), consisting of BN, GO, and α-Fe_2O_3, was ground into fine

powder and placed in sealed containers for subsequent characterization.

3. Characterization

3.1. Physicochemical characterization

The crystalline phase identification and particle size measurements were conducted using an X-ray diffraction (XRD) analysis utilizing an X'Pert Pro PANalytical diffractometer(UK) equipped with CuKα radiation of λ = 1.5406 Å, in a 2θ value between 20° to 80°. Approximately 3mg of the samples was sent for these analyses. We employed Field-Emission Scanning Electron Microscopy (FESEM) (SIGMA HV-Carl Zeiss, Germany) to characterize the surface morphology of the prepared composite. The material's structural properties were subsequently studied using Raman spectroscopy (Horiba XPLORA PLUS, France). The synthesized materials were subjected to thermal stability analysis under an inert nitrogen gas atmosphere utilizing a PerkinElmer Diamond TGA, USA. Fourier-transform infrared spectroscopy (FTIR) characterized the chemical bonding and functional groups of the composites based on an FTIR spectrophotometer, SHIMADZU IR Affinity-1, Japan. The optical characteristics, such as bandgap energy and electronic transitions, were investigated through UV-Visible spectroscopy employing a Carry 60 UV-Visible spectrometer, USA. These advanced characterization techniques provide the necessary insight to optimize the synthesized materials for their intended applications.

3.2. Electrochemical characterization

3.2.1. Electrochemical studies in a 3-electrode configuration system

To evaluate the BN@α-Fe_2O_3/GO composite as a potential electrode, its electrochemical properties were examined in a three-electrode system using 6M potassium hydroxide (KOH) as the electrolyte. The electrochemical characteristics were comprehensively analyzed via cyclic voltammetry (CV), galvanostatic charge-discharge (GCD) analysis, and electrochemical impedance spectroscopy (EIS), all performed on an OrigaLys OGF01A electrochemical workstation. A standard three-electrode cell was used, with an Ag/AgCl electrode serving as the reference and a platinum wire as the counter electrode. The working electrodes were fabricated by drop-casting the synthesized materials onto a graphite current collector. CV tests were executed at scan rates spanning between 10 to 100 mV/s while GCD measurements were conducted at current densities of 3 to $7Ag^{-1}$ respectively. Throughout all electrochemical measurements, the applied potential window was constantly maintained between 0 to 0.5 eV respectively.

3.2.2. Preparation of composite electrode based on BN@α-Fe_2O_3/GO dispersion

The working electrode was formulated by blending 80wt% of BN@α-Fe_2O_3/GO active material with 15 wt% conductive carbon and 5 wt% PVDF-HEP binder in a mortar and pestle. A drop or two of acetone was introduced to this mixture to achieve a smooth consistency. A drop-casting technique was employed to uniformly deposit the resulting slurry onto a 1 cm^2 graphite substrate. Subsequently, the electrodes were transferred to a vacuum oven at 80 °C and dried at overnight. This drying process was critical for evaporating residual solvent and ensuring robust bonding of the active layer. The active material mass loading on every electrode was kept between 0 and 1 mg. In electrochemical tests, 6 M KOH aqueous electrolyte was used for all experiments, and was conducted at ambient temperature.

The technical performance metrics for the three-electrode setup are calculated using the equations:

Specific capacitance, $\mathbf{C}_{SP} = \frac{I \times \Delta t}{m \times \Delta V}$ (F/g)..... (1)

Energy density, $\mathbf{E} = \frac{Specific\ capacititance \times (\Delta V)^2}{7.2}$ ($Wh\ kg^{-1}$)..... (2)

Power density, $\mathbf{P_D} = \frac{\boldsymbol{Energy\ density} \times 3600}{\Delta \boldsymbol{t}}$ (W kg^{-1}) ..... (3)

The equation employs, 'I' as the discharging current (A), 'Δt' discharge time (s), 'ΔV' potential range (V), and 'm' denotes the mass of the active material (g).

4. Results and discussions

4.1. Physicochemical characterization

The XRD studies of BN, GO, α-Fe_2O_3, and their hybrid composite, BN@α-Fe_2O_3/GO, depict critical information on the structural properties, phase compositions, and interphase interactions. Fig. 1 illustrates the XRD patterns of the materials. According to the literature, it is observed that a peak at 26.77^0 assigned to the (002) hkl crystal plane in BN structures, and is in agreement with the JCPDS card no 34-0421 respectively [18]. Additional peaks validate the high crystallinity and phase purity of BN. The XRD analysis of GO indicates a peak intensity at 10.93^0 corresponding with the (001) hkl plane, which is due to the interlayer spacing created from oxygen-containing functional groups [19]. The absence of a peak at approximately 26° suggested that successful oxidation and exfoliation had occurred. In terms of the XRD pattern, α-Fe_2O_3 showed clear peaks indicated at 33.2^0, matching the (104) hkl planes from a rhombohedral α-Fe_2O_3 phase. These reflections were in good agreement with the hematite rhombohedral structure JCPDS No: 01-084- 0307 confirming phase purity [20]. The BN@α-Fe_2O_3/GO hybrid composite exhibits the characteristic peaks of all three individual component materials, indicating the formation of a hybrid composite. The peak associated with GO is prominent, while the peaks from both BN and hematite are present as well. The intense broader peak at $2\theta \approx 10.40^0$ correlated with GO; meanwhile, the broader peaks are identified at $2\theta \approx 33.71^0$, 35.25^0, 40.08^0, 42.38^0, $49.70^{0,}$ $62.84^{0,}$ and $76.28^{0,}$ respectively. The intensity of the BN (002) peak at 26.98^0 was lower and displayed subtle evidence of peak broadening. The enhanced interfacial interactions within the hybrid system stem from the likely chemical bonding occurring between the metal center of α-Fe_2O_3. and the oxygen-bearing functional groups present on the GO surface. These hybridizations alter the long-range order of each component, resulting in peak broadening. The retention of the peaks from all three components suggests that their constituent crystalline structure has remained intact in the composite, and no new crystalline phases were formed under the synthesis conditions.

The next step was to further analyze quantitatively, to calculate average crystallite size (D), lattice strain (ε), and dislocation density (ρ) for each component. The Debye-Scherrer equation (shown below) was used to calculate the average crystallite size (D) of BN, GO, α-Fe_2O_3, and their hybrid composite, BN@α-Fe_2O_3/GO.

$$D=\frac{k\lambda}{\beta cos\theta} \quad (4)$$

where 'k' is the constant, X-ray wavelength (λ), the full width at half maximum (β) of the diffraction peak, and the Bragg angle (θ) respectively.

The crystallite sizes of the synthesized materials were calculated and found to be at the nanoscale. Furthermore, the respective lattice strain was also derived. Also, during the calculations, the dislocation density(ρ) to identify the concentration of defects and dislocations was measured as per the formula given below, and the data related to this are depicted in Table 1.

The dislocation density (ρ) is evaluated as,

$$\rho=1/D^2 \quad (5)$$

where 'D' is the average crystallite size.

Table 1. Quantifiable attributes of BN@α-Fe_2O_3/GO composite and its constituent materials based on XRD analysis.

Sample	**Average Crystallite size, D (nm)**	**Strain, ε (%)**	**Dislocation density, ρ × 10^{14} lines/m^2**
BN	47.24	0.181	4.47
GO	15.25	2.888	4.30
α-Fe_2O_3	22.23	0.428	2.30
BN@α-Fe_2O_3/GO (as in this reported work)	25.24	1.219	1.47

The crystallite dimension of BN@α-Fe_2O_3/GO hybrid composite is about 25.24 nm, which is between the larger BN crystallites and the smaller GO and α-Fe_2O_3 nanoparticles is considered an important indicator of a successful integration of components. The average crystallite size was notably greater than the values measured for GO and α-Fe_2O_3 showing that two-dimensional radii of the BN and GO lamellar structures acted as a confinement agent that governed the growth and distribution of α-Fe_2O_3 nanoparticles, thus limiting the excessive aggregation of smaller entities within the composite matrix. Thereby, BN@α-Fe_2O_3/GO results in a composite material fine-tuned for crystallite size, lattice strain, and defect density.

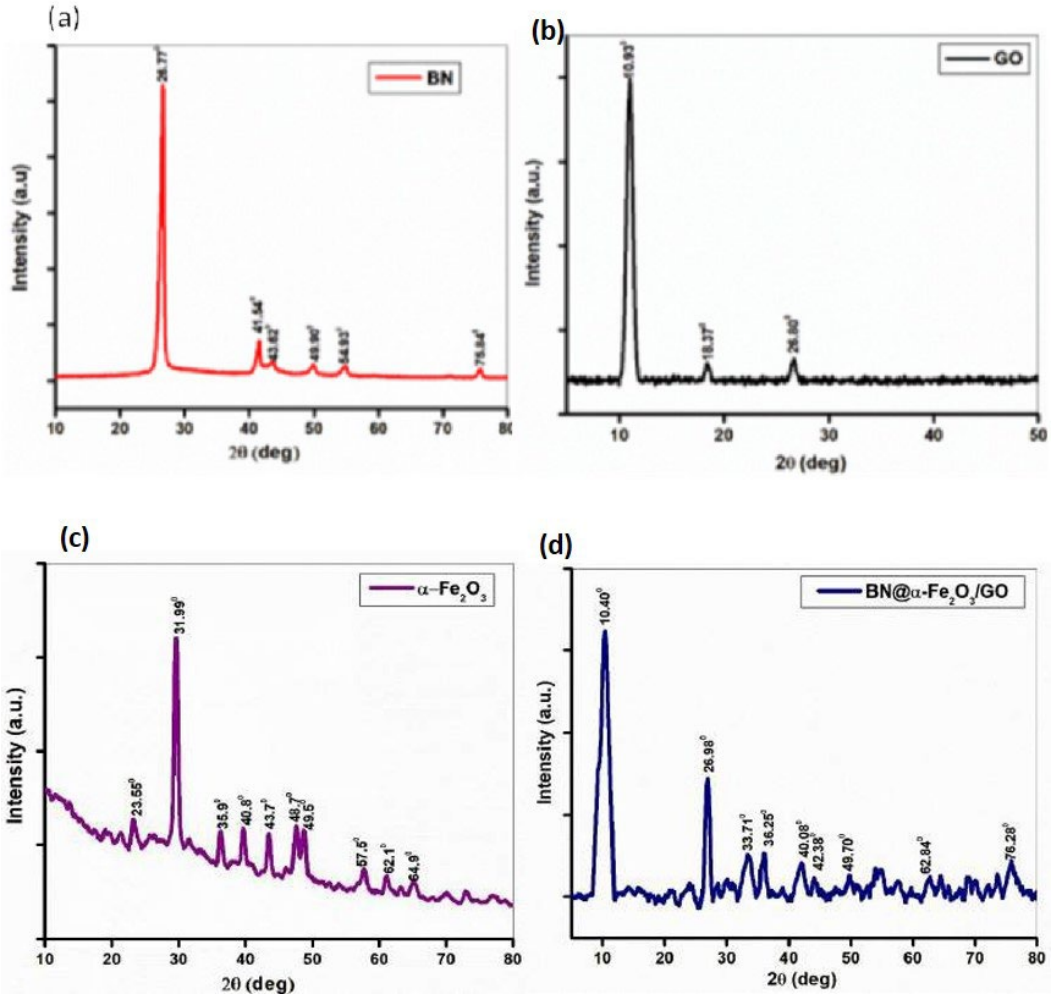

Fig. 1. The XRD analysis spectra of (a) BN, (b) GO, (c) α-Fe_2O_3, and (d) BN@α- Fe_2O_3/GO composite synthesized via the hydrothermal technique. XRD, X-ray diffraction; BN, boron nitride; GO, graphene oxide; α-Fe_2O_3, hematite .

The FTIR spectroscopy technique was employed to find the chemical functionalities of BN, GO, α- Fe_2O_3, and the ternary hybrid composite BN@α-Fe_2O_3/GO. All spectra were recorded across 4000–400 cm^{-1} and is illustrated in Fig. 2. The FTIR spectrum of BN exhibits two distinguishing absorption bands approximately at 1384.70 cm^{-1} and 813.85 cm^{-1} corresponding to the stretching and bending vibrations of B-N and B-N-B bonds within the hexagonal basal plane [21]. It is also noted that GO exhibits distinct absorption bands assigned to oxygen-rich functional groups resulting from the oxidation reaction (Fig. 2a). The broad peak at 3433.9 cm^{-1} represents the O-H stretching vibrations originating from surface hydroxyl groups and physically adsorbed water [22]. Furthermore, the C-H stretching vibrations from edge-located CH_2 groups are observable at 2921.7 cm^{-1}. Fig. 2b demonstrates the FTIR spectrum of hematite associated with vibrational modes, namely, Fe-O vibrational modes in the mid-range region. Specifically, the peak at 548.8 cm^{-1} is characteristic of the Fe-O stretching motion within the rhombohedral crystal lattice. The additional peaks at 1108.8 cm^{-1} 1394.4 cm^{-1}, and 1638.8 cm^{-1} are related to Fe-O-H bending as well as contributions from adsorbed water and hydroxyl groups on the material's surface [23].

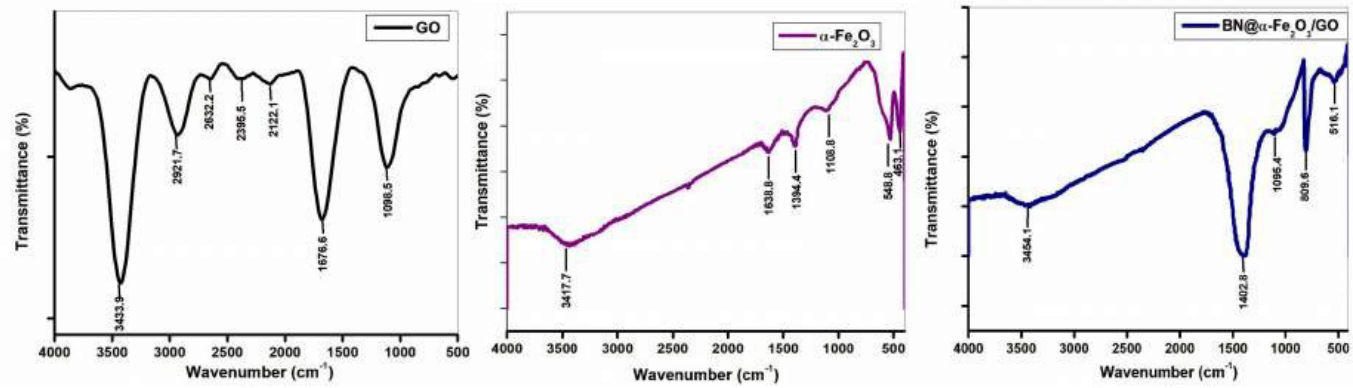

Fig. 2. The FTIR analysis graphs of (a) GO, (b) α-Fe_2O_3 and (c) BN@ α-Fe_2O_3/GO composite, respectively.

A peak at 3454.1 cm^{-1} in BN@ α-Fe_2O_3/GO composite corresponds to the vibrational mode of the hydroxyl O-H group. Still, overlapping with a similar region as that of GO and α-Fe_2O_3, which further indicates that hydroxyl functional groups are preserved (Fig. 2d). A distinct Fe-O absorption bands are observed at 516.1 cm^{-1}, emphasizing the integration of α-Fe_2O_3 nanoparticles. Furthermore, the persistence of Fe-O adsorption bands within the spectrum of the final hybrid composite confirms both the material's integration and the retention of its hematite structure. The peak at 809.6 cm^{-1} matches the vibrational modes of the B-N bonds. These overlapped shifted bands show key evidence for strong interaction at the interfaces and suggest the formation of new bonds in the composite phase. The slight shift or broadening of these bands implies interfacial interactions between the iron oxide nanoparticles and the BN/GO matrix. This includes the physicochemical interactions, such as surface capping by functional groups derived from GO and electrostatic interactions with the BN layers [24], that also induce some changes within the Fe-O bond environment, ultimately yielding the observed shifts and changes in BN@α-Fe_2O_3/GO composite. These results are an indication that the iron oxide nanoparticles are well-dispersed and closely associated with the surfaces of the 2D material, instead of simply appearing as isolated agglomerates.

The Raman spectral studies of the BN@α-Fe_2O_3/GO composite reveal information on the chemical structure, crystallinity, bonding environment, and phase composition, as in Fig. 3.

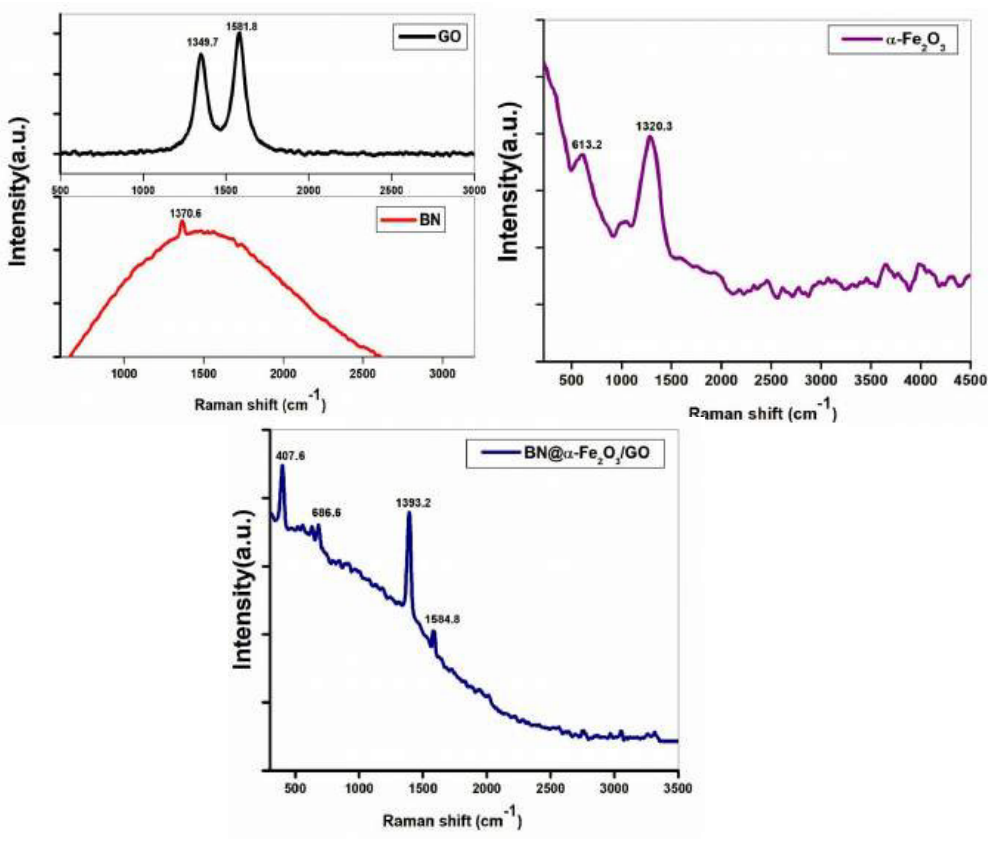

Fig. 3. The Raman analysis of spectra of (a)GO, (b) BN, (c) α-Fe_2O_3 and (d) BN@ α-Fe_2O_3/GO composite, prepared via hydrothermal synthesis.

The Raman spectral peaks for α-Fe_2O_3 appear between 613.2 cm^{-1} and 1320.3 cm^{-1} consistent with the published data (Fig. 3c). Furthermore, the analysis of GO, as per Fig. 3a, revealed two strong peaks, at 1349.7 cm^{-1} and 1581.8 cm^{-1} corresponding to D and G bands. The D-band is assigned to the A_{1g} vibrational mode, indicating the presence of structural defects and disorder in the carbon lattice. Conversely, the G-band confirms the presence of sp^2-hybridized carbon (the E_{2g} phonon mode), arising from disordered carbon atoms [25]. The Raman spectrum for BN exhibits a characteristic peak at 1370.6 cm^{-1} which is assigned to the in-plane E_{2g} vibrational mode of the B-N bonds as in Fig. 3b [26]. The vibrational peaks of BN also overlap with the intensity and peak position in BN@α- Fe_2O_3/GO composite. The Raman spectrum of the BN@α-Fe_2O_3/GO composite demonstrates several alterations that corroborate the development of a hybrid material (Fig. 3d). Specifically, the emergence of new peaks at 407.6 cm^{-1} and 686.6 cm^{-1} is associated to the A_{1g} and E_g modes of α-Fe_2O_3, respectively, related to the symmetric Fe-O stretch, and bending vibrational modes, respectively. These features demonstrate that α-Fe_2O_3 nanoparticles are incorporated into the composite. Furthermore, the D-band and G-band of the GO component display subtle displacements. The D-band observed at 1393.2 cm^{-1} and the G-band observed symmetric mode at 1584.8 cm^{-1} both experience slight shifts compared to GO; these shifts are attributed to strain, as explained during XRD analysis within the hybrid. The overlapping of the BN vibrational mode with the D-band of the GO causes an upshift of the D-band in the composite, resulting in strong electronic coupling and interfacial interactions [27]. These changes demonstrate a structurally integrated hybrid system where lattice vibrations are changed through the phonon confinement. The presence of Fe-O related peaks, changes to GO bands, and merging of BN features collectively support the synergistic interactions and substantial hybridization of BN@α-Fe_2O_3/GO composite, all of which indicate increased tunable properties for energy storage applications.

Thermogravimetric Analysis (TGA) is conducted to evaluate a material's thermal decomposition and stability by recording the accompanying changes in weight and composition during the heating process. Fig. 4 exhibits the TGA weight loss curves of the samples. BN exhibits high thermal endurance, as evidenced by its TGA profile which displays only a minor mass loss and

subtle degradation, indicating that BN has notable thermal stability owing to its strong B-N covalent bonding network and due to its low chemical reactivity in a nitrogen atmosphere [28]. As evidenced by literature and experimental work, GO exhibits a multi-step pathway of thermal decomposition, where the initial mass loss occurs below 100 ^{0}C followed by the significant weight loss at the range of 150–300 ^{0}C, linked to the cleavage of oxygen-bearing surface groups such as hydroxyl, carboxyl, and epoxy functionalities [29]. All of these functional groups are thermally labile, and thus, the loss of gas as these functional groups are removed will result in rapid structural collapse. The TGA analysis also depicts that GO typically undergoes a weight loss of about 30%–40% owing to its low thermal resistance [30]. The thermal studies of α-Fe_2O_3 show that a mass loss is correlated to the loss of lattice hydroxyl groups in the sample and surface adsorbed water moisture. The weight becomes stabilized past this temperature, indicating that the α-Fe_2O_3 phase shows high thermal robustness to increased temperature regimes [31]. The TGA profile of the BN@α-Fe_2O_3/GO composite, as in Fig. 4a, indicates a substantial improvement in thermal behavior with a total weight loss of only 5.62% up to 700 ^{0}C, significantly lower than GO and α-Fe_2O_3 materials. The enhanced thermal stability is a result of synergistic interactions between the three components. It is observable that the incorporation of BN, a thermally stable material in into BN@α-Fe_2O_3/GO composite acts as a physical shield against volatile decomposition and heat- induced decomposition of GO. The α-Fe_2O_3 nanoparticles also chemically bind to the oxygen functionalities on GO by Fe-O-C and Fe-O-B bonding, thus improving the lattice stability and decreasing the free oxygen availability for the decomposition process. Moreover, the stacked architecture of the BN and GO components limits internal heat flow, thus enhancing the material's thermal stability and resistance to degradation.

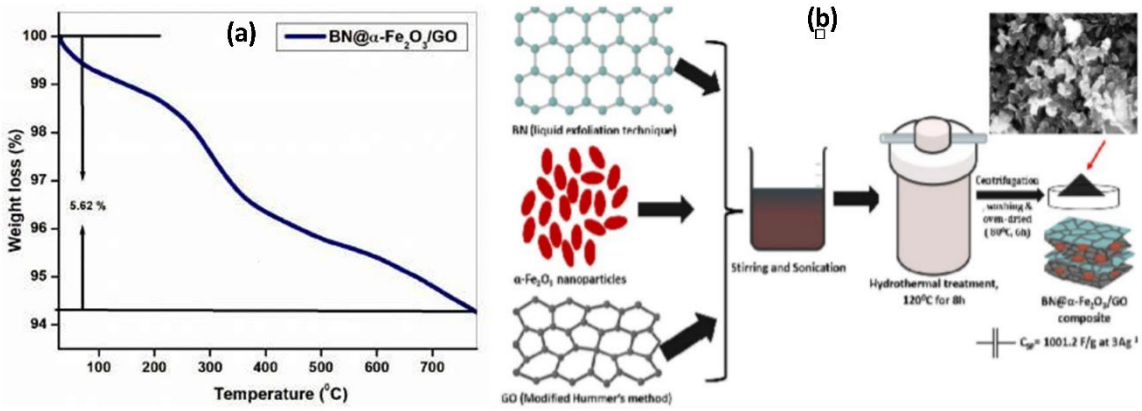

Fig. 4. (a) The TG analysis BN@ α-Fe_2O_3/GO composite, prepared via hydrothermal synthesis and (b)The schematic hydrothermal synthesis of BN@ α-Fe_2O_3/GO composite.

The UV-Visible spectral studies of BN, GO, α-Fe_2O_3, and BN@α-Fe_2O_3/GO composite is illustrated in Fig. 5, investigating electronic transitions within the constituent materials, thus providing information on the optical properties, bandgap energies, etc.

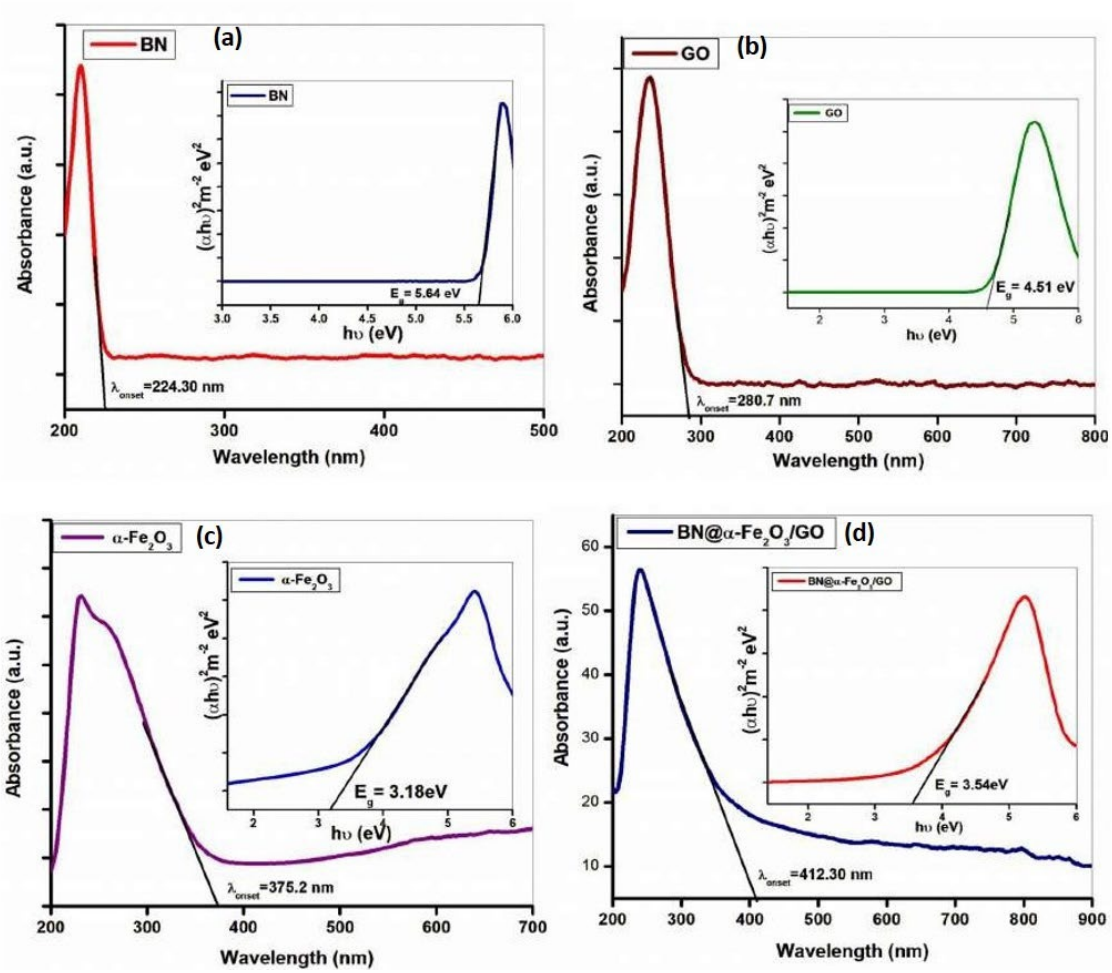

Fig. 5. The UV-Visible analysis spectra and their corresponding Tauc plots (in inset) of (a)BN, (b) GO, (c) α-Fe_2O_3, and (d) BN@ α-Fe_2O_3/GO composite, synthesized through the hydrothermal treatment.

The bandgap energies for the synthesized composites were calculated using the specified equation, utilizing the onset wavelength (λ_{onset}) data acquired from UV-Vis spectroscopy.

$$E_g = hc/\lambda_{onset} \quad (6)$$

In this context, 'h', 'c', and 'λ_{onset}' represent the Planck's constant, the speed of light, and the wavelength corresponding to absorption onset, respectively. The respective Tauc plots as insets provide the bandgap values using the given equation,

$$(\alpha h\upsilon)^2 = A(h\upsilon - E_g) \quad (7)$$

Where 'α' stands for absorption coefficient, 'hυ' signifies the photon energy, and 'E_g' corresponds to the optical bandgap.

BN exhibits a strong adsorption peak at 224.30nm, typically occurring due to the π-π* electronic transitions between boron and nitrogen atoms in BN, as shown in Fig. 6a. The wide optical bandgap of BN is observed at 5.64 eV (inset of Fig. 5a), which agrees readily with the values associated in existing literature of BN [32], establishing the electronegativity differences between the B and N atoms, resulting in poor delocalization of electrons. The major absorption peak in GO is at 230.5 nm (λ_{onset}= 280.7 nm) and is related primarily to the π-π* electronic transitions of the isolated aromatic sp^2 domains in the GO sheets (Fig. 5b). The oxidation process introduces oxygen functionalities, which disrupt the extended π-conjugation system found in pristine graphene. The Tauc plot (inset of Fig. 5b) predicts an optical bandgap of 4.51 eV, indicating that GO possesses a much smaller bandgap than BN, due to localized electronic states, and its restored partial π-conjugated structure [33]. Fig. 5c and the inset represent the adsorption spectrum and Tauc plot of α-Fe_2O_3, with an absorption onset at 375.2nm and a bandgap of 3.3 eV [34], respectively, which is in agreement with the spectroscopic data and bandgap calculations as provided in Table 2.

Table 2: Determination of optical bandgap via spectral analysis and Tauc method for BN, GO, α-Fe_2O_3, and their composite.

Sample	Absorption Onset wavelength, λonset values (nm)	Bandgap Energy determination from spectral analysis (eV)	Tauc plot, Bandgap energy (eV)	Bandgap values from reported literature (eV)
BN	224.3	5.52	5.64	5-6 [35]
GO	280.7	4.41	4.51	3.2- 4.1 [36]
α-Fe_2O_3	375.2	3.30	3.18	2.1-3.2 [37]
BN@α-Fe_2O_3/GO (as in this Reported work)	412.3	3.00	3.54	-

The UV-Vis absorption spectrum (Fig. 5d) of the BN@α-Fe_2O_3/GO composite exhibits a complex layering of the electronic properties of each component present within the composite, showing notable differences in the adsorption profiles and bandgap energies of individual components. The composite depicts a broad absorption profile ranging from the UV to visible region with an absorption onset of approximately λ_{onset} = 412.3nm. The close interface of GO and BN creates significant electronic interaction. GO underwent partial reduction during the hydrothermal synthesis, restoring some π-conjugation. This effectively decreases the energy of its π-π^* transitions and enhances the electronic binding interactions at the interface of α-Fe2O3 and BN, thereby creating new and lower-energy electronic transitions across the interfaces [38]. The interfaces formed by the semiconducting α-Fe_2O_3 and GO (narrow bandgap semiconductor) and the insulating BN also created different types of heterojunctions, which caused the formation of new energy levels at the interfaces. Based on the FTIR and Raman results, it is apparent that different interactions take place between the constituent materials. Using the absorption properties, absorption data were analyzed via the Tauc plot (inset of Fig. 5d) to calculate the band gap, yielding an E_g of 3.54 eV for BN@α-Fe_2O_3/GO composite. These types of interactions initiate charge transfer pathways for efficient electron-hole separation and transfer across heterojunctions [39].

The FESEM analysis served as the technique for evaluating the surface structure and microstructural characteristics of synthesised BN@α-Fe_2O_3/GO composites. The FESEM micrographs of the composite were taken at sequential magnifications, 75KX, 100KX, 15OKX, and 200KX. consecutively. The FESEM images of the BN@α-Fe_2O_3/GO composite (Fig. 6) obtained at lower and higher magnifications show a heterogeneous multi-component morphology, giving a strong visual representation of the successful integration of the separate components. At lower magnifications (Fig. 6, Top row), the entire composite material appeared as a dense aggregated network of sheet-like structures intermixed with nanoparticles. Upon increasing the magnification, the detailed architecture of this composite (Fig. 6, bottom row) is visible.

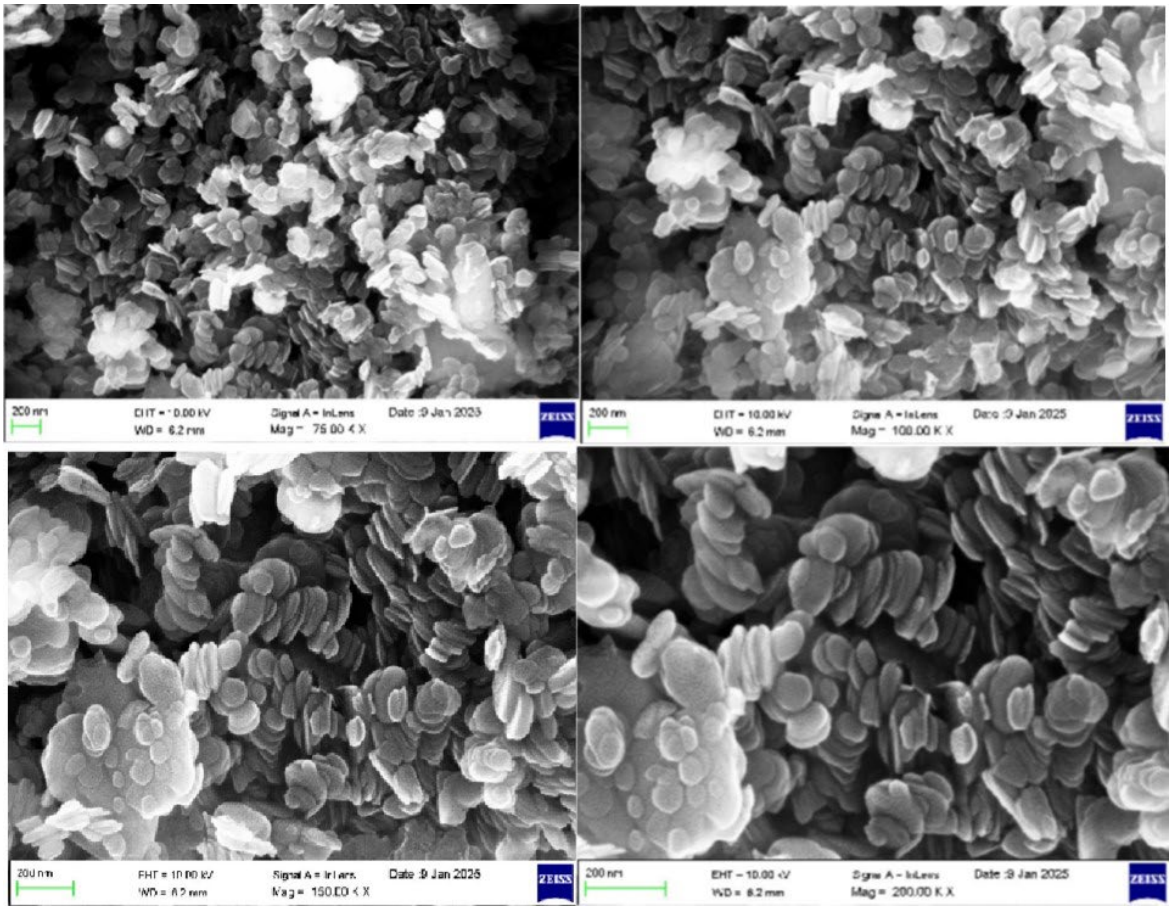

Fig. 6. The FESEM images of hydrothermally prepared BN@α-Fe_2O_3/GO composites captured at different resolutions (75KX, 100KX, 15OKX, and 200KX), respectively.

The thin, crumpled, and folded sheet-like morphologies exhibit the characteristics of two-dimensional (2D) materials that consist of GO and BN sheets. Numerous α-Fe_2O_3 nanoparticles appear to be homogeneously distributed, while appearing to be physically anchored, with a relatively constant size and irregular shapes that resemble rounded or pseudo-spherical shapes. The FESEM images also reveal further visual confirmation that these nanoparticles are not strictly agglomerated in isolation, but instead are dispersed and integrated effectively onto the surfaces of the GO and BN sheets. This intimate association of particles with sheets is crucial for maximizing interfacial contact and physical dimensionality of the surface area of the components. [40] BN@α-Fe_2O_3/GO composite possesses an average particle size estimated between 15–50 nm. To maximize ion adsorption and support sufficient redox reactions, materials must feature a significant, readily available surface area that provides multiple active sites. The observable porous, crumpled, and highly interconnected morphology of both BN and GO suggests a large electrochemically active surface area, which promotes the diffusion and adsorption of electrolyte ions. The observed interconnected pores and open channels are very important for fast and effective transport of electrolyte ions to/from the active material surfaces, thereby reducing the resistance to ion diffusion, which is a major limitation when discussing the rate capability and power density of supercapacitors. In addition to this, rough surface morphology and hierarchy initiated the addition of electroactive sites, thus contributing improved the charge storage behavior. Since α-Fe_2O_3 nanoclusters are uniformly dispersed and no large-scale agglomeration is noted, it is evident that a controlled synthesis process has occurred, which also preserved the nanoscale interactions associated with each component of the composite.

4.2. Electrochemical characterizations

The electrochemical performance and characteristic features of an active material are significantly influenced by its structural properties and morphologies. The electrochemical performance of the hydrothermally synthesised BN@α-Fe_2O_3/GO composite electrodes was

investigated. The electrochemical response of BN@α-Fe_2O_3/GO composite was characterized via CV analysis by varying the scan rate within a fixed potential range of 0 to 0.5V, as depicted in Fig. 7a. The quasi-rectangular curve observed at low sweep rates confirms the presence of significant electric double-layer capacitance (EDLC). This phenomenon stems from non-Faradaic interactions established at the electrode/electrolyte interface. It is evident that both GO and BN exhibit high specific surface area and have a layered structure, which initiates active ion adsorption, thus contributing to the stability and capacitive response of the composite [41]. α-Fe_2O_3 nanoparticles in the composite ensure redox chemistry, exhibiting pseudocapacitive behavior [42]. As the scan rate was raised from 10 mV/s to 100 mV/s, a clear increase in the enclosed area of the cyclic voltammetry (CV) curves was observed. This behavior is characteristic of a capacitive charge storage mechanism. Importantly, the quasi-rectangular shape is retained while the broad peaks are apparent even at faster scan rates. The observed stability suggests the composite can endure continuous charge/discharge cycles without structural degradation. Crucially, the synergistic effect between the constituents serves to boost the overall electrochemical activity of the resulting material.

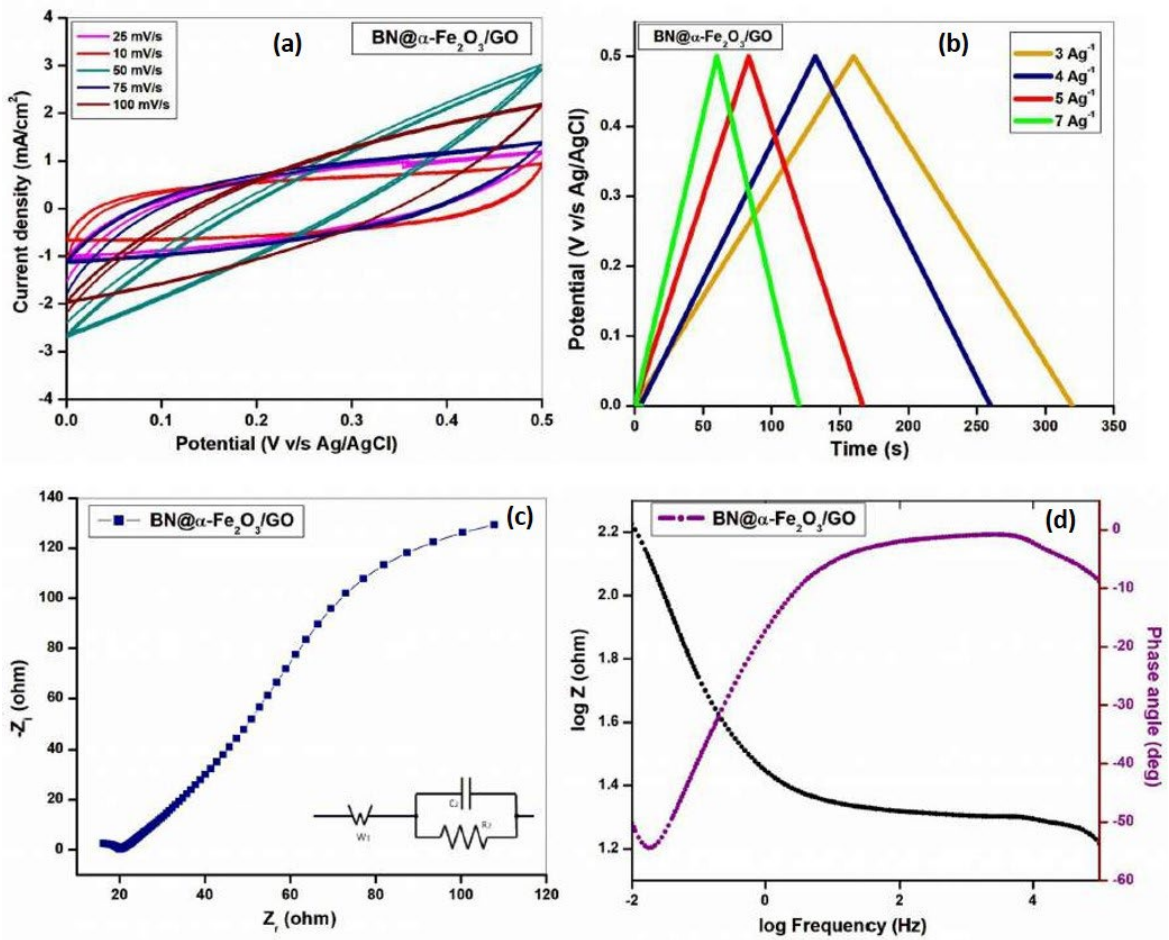

Fig. 7. The electrochemical performance of electrodes synthesised with BN@α-Fe_2O_3/GO composite-(a) The CV analysis at varying scan rates, (b) The GCD curves at different current densities, (c) The Nyquist plot, and the inset displays the equivalent circuit, and (d) The Bode plot of the composite, respectively. GCD, galvanostatic charge-discharge; CV, cyclic voltammetry.

The GCD testing of BN@α-Fe_2O_3/GO composite under varying current densities (3, 4, 5, and 7 Ag^{-1}) is evaluated using a three-electrode cell in a 6 M KOH aqueous electrolyte. The GCD studies elucidate key information on the storage ability and electrochemical efficiency of the synthesized sample. Fig. 7b demonstrates the GCD curves of the hydrothermally synthesised composite. The symmetric triangular shape observed in the GCD of BN@α-Fe_2O_3/GO composite and an almost linear voltage-time relationship, denotes typical capacitive behavior, which is controlled by EDLC nature and pseudocapacitance by α-Fe_2O_3. The specific capacitance (C_{SP}) at

current densities of (3, 4, 5 and 7 Ag^{-1}) was calculated using Eq. (1) and is noted as 1001.2 F/g, 971.5 F/g, 815.9 F/g, and 808.78 F/g, which is comparatively higher considered to its constituent materials, BN (20 to 90F/g), GO (140 to 160 F/g) and α-Fe_2O_3 (193 F/g to 730F/g). A reduction in C_{SP} correlates directly with an increase in current density. This correlation is largely governed by the kinetically limiting factors of ion diffusion and the finite supply of electrolyte available for faradaic reactions during high-rate cycling [43]. To assess the practical applicability of BN@α- Fe_2O_3/GO composite electrodes in supercapacitor applications, the corresponding energy density (E) and power density (P_D) were determined, and the calculations were carried out accordingly using Eq. (3) and Eq. (4), as these factors reflect how this composite material acts as a power source. BN@α-Fe_2O_3/GO composite and those recent composites reported in the literature are compared using a Ragone plot, as in Fig. 8d. As calculated, the BN@α-Fe_2O_3/GO composite yielded an energy density of 34.76 Wh kg^{-1} at a power density of 750 W kg^{-1} at 3Ag^{-1}. With increasing current densities, the energy densities of the composite slightly decreased to 33.73Wh kg^{-1}, 28.33Wh kg^{-1}, and 28.08Wh kg^{-1} for current densities of 4Ag^{-1}, 5Ag^{-1}, and 7Ag^{-1}, whereas the corresponding power densities increased to 1000W kg^{-1}, 1250W kg^{-1}, and 1750W $kg^{-1,}$ respectively. The BN@α-Fe_2O_3/GO hybrid retained 82.7% of its capacitance after 10000 cycles (Fig. 8b), inferring the outstanding cyclic stability of the device. A comparative evaluation based on the electrochemical analysis of the current BN@α-Fe_2O_3/GO composite with recent literature is outlined in Table 3.

Electrochemical Impedance Spectroscopy (EIS) measurements were performed to determine the electrochemical behavior and interfacial properties of the BN@α-Fe_2O_3/GO composite. The frequency range selected for this analysis spanned from 100 kHz to 0.01 Hz. The Nyquist plot displays an inclined linear segment at lower frequencies, and a compressed semicircle is observed in the high-frequency domain, as illustrated in Fig. 7c. The solution resistance (R_s) primarily originates from the combined resistance of the electrolyte, the electrode material, and the current collector, and is indicated by the high-frequency intercept on the real axis (Z_r). Here, R_s ranges from 15 to 20Ω, and it corresponds to the initial intersection of the semicircle with the real axis in the Nyquist plot. A reduced semicircle diameter provides clear evidence of both rapid redox kinetics and low interfacial resistance between the electrode and the electrolyte, which denotes a low charge transfer resistance (R_2 = 500 mΩ). The controlled ion diffusion within the electrode matrix is represented by the Warburg impedance (W_I), shown as an inclined line at lower frequencies, facilitating smooth transport of electrolyte ions within the material composite, which is advantageous for supercapacitor electrodes.

Table 3. A comparative assessment of the electrochemical metrics of BN@α-Fe_2O_3/GO composites with existing supercapacitor composite materials.

Composite material	Preparation method used	Specific capacitance (Fg^{-1})	Energy density (Wh kg^{-1}) at Power density (W kg^{-1})	Cyclic stability (Retention rate with no.of Cycles) (ref)
BN@α-Fe_2O_3/GO (Present work)	Hydrothermal	1001.2 F/g at 3Ag^{-1}	34.76 Wh kg^{-1} at 750 W kg^{-1}	82.7% after 10000 cycles.
h-BN /MoS_2	Hydrothermal	411.5F/g at 10mV/s	46.1 Wh kg^{-1} at 844.9 W kg^{-1}	86% after 2000 cycles [44]
BN/Bi_2S_3	Hydrothermal	779.9F/g at 10mV/s	69.68 Wh kg^{-1} at 1689.7 W kg^{-1}	94.3% after 5000 cycles [45]
MOS_2/GO/BN	Hydrothermal	329F/g at 0.5Ag^{-1}	36.5 Wh kg^{-1} at 1043 W kg^{-1}	94% after 10000 cycles [46]
$CoMoO_4$@BN	Hydrothermal, Ball milling	1682.7F/g at 1 Ag^{-1}	51.2Wh kg^{-1} at 600W kg^{-1}	96% after 2000 cycles [47]

Phosphate-α-Fe_2O_3 /rGO	Solvothermal Calcination	586.6F/g at 1Ag^{-1}	82 Wh kg^{-1} at 1200 W kg^{-1}	95% after 20000 cycles [48]
Tin-doped α-Fe_2O_3	Hydrothermal	832F/g at 10mV/s	28.3 Wh kg^{-1} at 528.8 W kg^{-1}	80% after 1000cycles [49]
rGO/ NiMnCo	Electrophoretic process	59.17F/g at 1Ag^{-1}	66.9 Wh kg^{-1} at 800 W kg^{-1}	90 % after 3000cycles [50]
rGO/ $NiFe_2Se_4$	Hydrothermal	1046F/g at 1Ag^{-1}	30 Wh kg^{-1} at 227 W kg^{-1}	89% after 5000cycles [51]

The frequency-dependent behavior of the BN@α-Fe_2O_3/GO composite is illustrated in the Bode plot in Fig. 7d. The observed decrease in the magnitude of impedance (log |Z|) as frequency rises is a characteristic behavior for capacitive systems. At higher frequencies, R_s becomes the primary contributor to total impedance, while at lower frequencies, the combined effects of CPE behavior and ion diffusion through the porous matrix dominate. The phase angle plot shows a peak of about -65^0, indicating a deviation from ideal capacitive behavior (-90^0). The relatively mild phase shift suggests a hybrid storage mechanism, where both surface ion adsorption and Faradaic redox reactions contribute to the overall capacitance. The phase angle nearing -90^0 at low frequencies confirms the prevailing capacitive character, indicating a high charge storage capability with low energy dissipation, which is characteristic of a good supercapacitor material [52]. The BN@α-Fe_2O_3/GO composite demonstrates a synergistic hybrid of both capacitive and Faradaic storage mechanisms. GO plays a crucial role in ensuring fast electronic conductivity and electric double-layer capacitance owing to its large surface area and superior conductivity. Meanwhile, BN contributes mechanical stability, thermal resistance, and helps with the agglomeration of active species. α-Fe_2O_3, being redox-active, participates in surface-confined Faradaic processes, significantly increasing the pseudocapacitive contribution. The low interfacial resistance (R_2 = 0.5 Ω), high interfacial capacitance, and prominent Warburg diffusion behavior all indicate that the composite promotes rapid ion/electron transport. The conducting network established by GO, supported by BN, enhances the pathways for the swift. movement of ions. These characteristics are essential for achieving superior energy and power density, as demonstrated through GCD studies, as well as ensuring long cycling stability in supercapacitor devices.

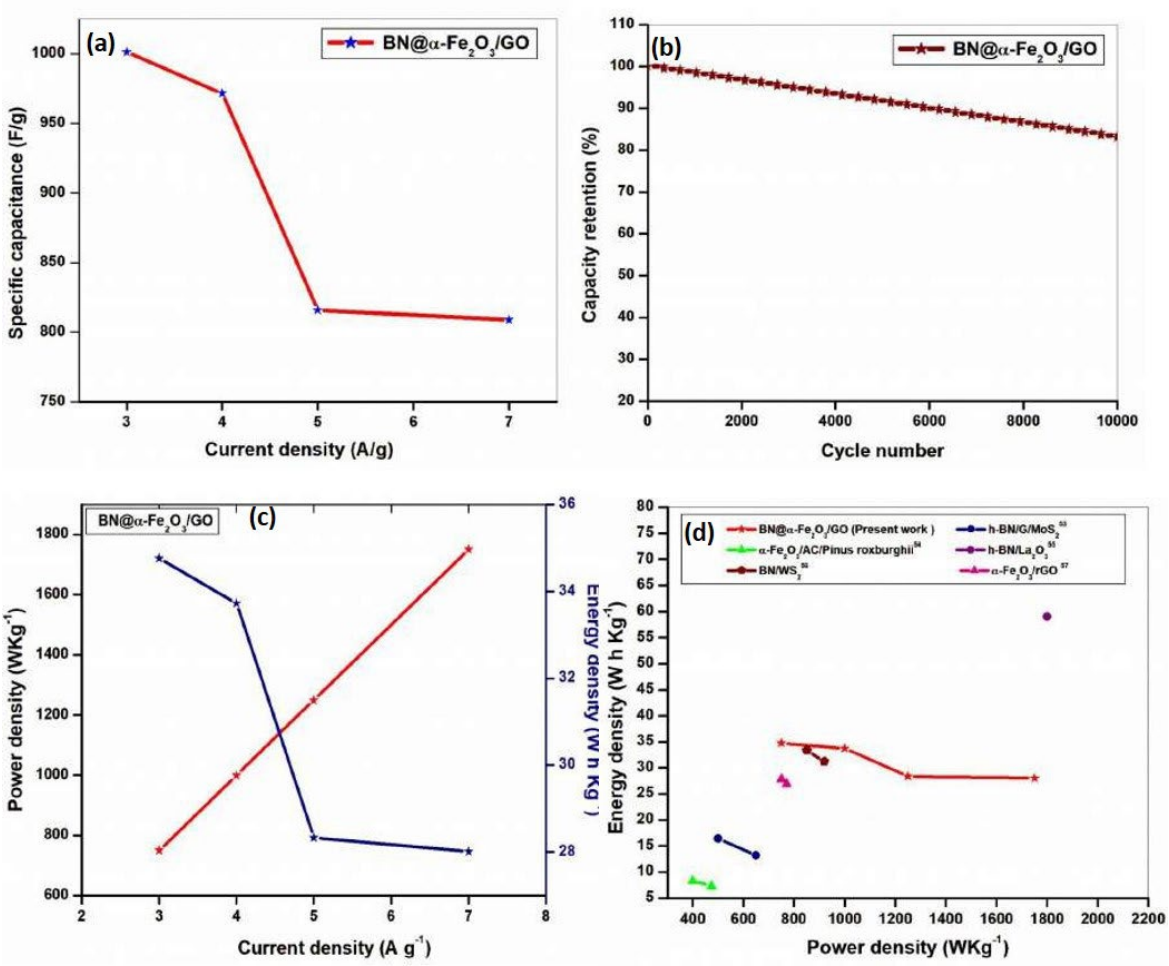

Fig. 8. (a) The variation of specific capacitance of BN@α-Fe₂O₃/GO composite in terms of current density. (b) Assessment of cyclic performance of hydrothermally synthesised BN@α-Fe₂O₃/GO composite, showcasing the cyclic stability up to 10000th cycle. (c) The relationship between power density and energy density of the prepared composite with current density. (d) The Ragone plot represents the comparison of energy and power densities between the present BN@α-Fe₂O₃/GO composite with previously reported materials.

Fig. 8a depicts the dependence of specific capacitance on varying applied density from 3 to 7 Ag^{-1}. The observed decrease in performance, as shown in this plot, is characteristic of high-performance supercapacitor electrodes. This trend is generally attributed to restricted ion diffusion and diminished electrolyte accessibility when operating at higher current densities. When operating at low current densities, the diffusion and intercalation of ions can thoroughly access all active sites within the electrode material. This comprehensive utilization of the active material is what leads to the observation of a higher specific capacitance [58]. However, an increase in the current density leads to insufficient time for ion transport, preventing the full utilization of the active material. This incomplete engagement is directly reflected in the corresponding drop in observed capacitance. Despite this, the BN@α-Fe2O3/GO composite maintained 82.7% of its capacitance at more than doubled current density (3 to 7 A g^{-1}), representing enhanced rate capability. The inverse relation of energy vs power density is a usual phenomenon observed in electrochemical capacitors [59]. Overall, the data in Fig. 8c indicate that the BN@α-Fe2O3/GO hybrid composite achieves a desirable combination of both a high amount of energy stored (and in turn high power delivered), an important characteristic of a next-generation supercapacitor system. The findings conclusively demonstrate that the BN@α-Fe2O3/GO hybrid composite exhibits outstanding electrochemical performance. This renders it an appropriate electrode material for supercapacitors and affirms its promise for the development of highly efficient energy storage devices.

5. Conclusions

A multifunctional BN@α-Fe_2O_3/GO hybrid composite is successfully synthesized by the hydrothermal route. The physicochemical characterizations reveal the combination of a highly conductive, high-surface-area network, providing details on the structural, electrical, and chemical nature of the composite. The morphology studies of BN@α-Fe_2O_3/GO hybrid composite are evaluated by FESEM analysis. The composite also indicates the advantage of the individual properties exhibited by their constituents present, BN contributing high thermal and mechanical stability, GO offering high surface area, and α-Fe_2O_3 ensuring high theoretical capacitance by way of an increase in the number of active sites. The homogeneous mixing and intimate interfacial contact between the constituents enabled effective charge transport and ion diffusion on the electrode surface, as confirmed through morphological and structural examination. The performance of the BN@α-Fe_2O_3/GO electrode was electrochemically studied to evaluate the characteristics of the resulting cell. The highest specific capacitance value recorded from the GCD studies is 1001.2F/g at $3Ag^{-1}$ for 6M KOH, respectively. Correspondingly, the energy density is calculated, and the power density of BN@α-Fe_2O_3/GO composite is evaluated and found as 34.76 Wh kg^{-1} at a power density of 750 W kg^{-1}. The BN@α-Fe_2O_3/GO composite also displayed exceptional cyclic stability and sustained about 82.7% of its specific capacitance even after 10000 cycles. The superior electrochemical performance observed in the composite is attributed to the interactions of individual GO, BN, and α-Fe_2O_3 materials. Even after these in-depth analyses, a little structural and morphological deterioration of the deposited materials was witnessed, unveiling the device's long-term performance and durability. The outcomes of this investigation study unveil the outstanding potential of the BN@α-Fe_2O_3/GO composite. The results affirm the material's suitability for use in next-generation energy storage applications. The synergic interactions between the constituent materials have opened the door to outstanding performance, which has rendered this composite a potential candidate for advanced electrochemical devices.

Availability of Data and Materials

The datasets generated and analyzed during the current study can be obtained from the corresponding author following a reasonable request.

Author Contributions

SS: Methodology, Formal analysis, Writing – original draft, Investigation, Data curation. BB: Writing – review & editing, Investigation, Supervision, Funding acquisition, Conceptualization.

Acknowledgements

The authors sincerely acknowledge and convey their sincere gratitude towards the institutional support shown by Noorul Islam Centre for Higher Education, Tamil Nadu. This research was financially supported by the Department of Science and Technology (DST), New Delhi, through the research fellowship (IF190811), in carrying out this research work.

Funding

This research was carried out with financial support from the Department of Science and Technology (DST), New Delhi, specifically through the provision of a research fellowship (IF190811).

Conflict of Interest

All authors certify that they have no conflicts of interest or professional relationships that might inappropriately affect the results presented in this research.

References

[1] H. R. Khan, A. L. Ahmad, Journal of Industrial and Engineering Chemistry **134**, 1(2024). https://doi.org/10.1016/j.jiec.2024.01.012
[2] B. Chettiannan, E. Dhandapani, G. Arumugam, R. Rajendran, M. Selvaraj, Coordination Chemistry Reviews **518**, 216048(2024). https://doi.org/10.1016/j.ccr.2024.216048
[3] D. R. Lobato-Peralta, P. U. Okoye, C. Alegre, Journal of Power Sources **617**, 235140(2024). https://doi.org/10.1016/j.jpowsour.2024.235140
[4] S. Gautam, S. Rialach, S. Paul, N. Goyal, RSC Advances **14**(20), 14311(2024). https://doi.org/10.1039/D4RA01345K
[5] S. Shams, B. Bindhu, ES Energy & Environment **24**, 1160(2024). https://doi.org/10.37256/ese.1242024.1160
[6] R. Y. Tay, H. Li, H. Wang, J. Lin, Z. K. Ng, R. Shivakumar, E. H. T. Teo, Nano Today **53**, 102011(2023). https://doi.org/10.1016/j.nantod.2023.102011
[7] O. J. Ajala, J. O. Tijani, M. T. Bankole, A. S. Abdulkareem, Environmental Nanotechnology, Monitoring & Management **18**, 100673(2022). https://doi.org/10.1016/j.enmm.2022.100673
[8] M. Tahir, M. Fakhar-e-Alam, M. Atif, G. Mustafa, Z. Ali, Journal of King Saud University - Science **35**(5), 102695(2023). https://doi.org/10.1016/j.jksus.2023.102695
[9] S. Bhattacharjee, D. Seth, Langmuir **40**(1), 772(2023). https://doi.org/10.1021/acs.langmuir.3c02987
[10] C. S. Bongu, M. Arsalan, E. H. Alsharaeh, ACS Omega **9**(13), 15294(2024). https://doi.org/10.1021/acsomega.3c09932
[11] C. K. Maity, A. Sood, R. Singhmar, J. H. Choi, A. Milton, S. M. Choi, S. S. Han, Journal of Alloys and Compounds **1014**, 178734(2025). https://doi.org/10.1016/j.jallcom.2024.178734
[12] S. Sengupta, M. Kundu, ACS Applied Energy Materials **7**(9), 4243(2024). https://doi.org/10.1021/acsaem.4c00215
[13] M. Mumtaz, A. Mumtaz, F. Nasim, M. Sajid, Materials Chemistry and Physics **329**, 130035(2025). https://doi.org/10.1016/j.matchemphys.2024.130035
[14] S. Shams, B. Bindhu, A. Murali, R. Ramesh, A. Al Souwaileh, S. S. Han, Nanoscale Advances **7**, 1803(2025). https://doi.org/10.1039/D4NA00987K
[15] C. Gautam, S. Chelliah, RSC Advances **11**(50), 31284(2021). https://doi.org/10.1039/D1RA05845A
[16] V. O. Kotsyubynsky, V. M. Boychuk, I. M. Budzuliak, B. I. Rachiy, R. I. Zapukhlyak, M. A. Hodlevska, A. A. Malakhov, Physics and Chemistry of Solid State **22**(1), 31(2021). https://doi.org/10.15330/pcss.22.1.31-38
[17] M. S. Hafizuddin, C. L. Lee, K. L. Chin, P. S. H'ng, P. S. Khoo, U. Rashid, Polymers **13**(22), 3954(2021). https://doi.org/10.3390/polym13223954
[18] F. Zhang, Y. Sun, R. Xiang, D. Zhang, Z. Chen, F. Liu, S. Liu, Materials Research Bulletin **176**, 112824(2024). https://doi.org/10.1016/j.materresbull.2024.112824
[19] S. Zainab, M. Azeem, S. U. Awan, S. Rizwan, N. Iqbal, J. Rashid, Scientific Reports **13**(1), 6954(2023). https://doi.org/10.1038/s41598-023-34156-8
[20] S. M. Anas, C. C. Reddy, National Symposium on High Voltage-Energy Storage Capacitors and Applications, Springer Nature Singapore, 405(2023). https://doi.org/10.1007/978-981-99-2865-1_36
[21] S. Shaybanizadeh, A. N. Chermahini, Ceramics International **47**(8), 11122(2021). https://doi.org/10.1016/j.ceramint.2020.12.214
[22] M. Ebrahimi Naghani, M. Neghabi, M. Zadsar, H. Abbastabar Ahangar, Scientific Reports **13**(1), 1496(2023). https://doi.org/10.1038/s41598-023-28645-6
[23] S. Kumar, A. Kumar, T. Malhotra, S. Verma, Journal of Alloys and Compounds **904**, 164006(2022). https://doi.org/10.1016/j.jallcom.2022.164006
[24] L. L. Ye, X. Chen, Y. Chen, X. Yan, X. J. Guo, W. Z. Lang, Desalination **565**, 116824(2023). https://doi.org/10.1016/j.desal.2023.116824
[25] M. Sharma, S. Rani, D. K. Pathak, R. Bhatia, R. Kumar, I. Sameera, Carbon **184**, 437(2021). https://doi.org/10.1016/j.carbon.2021.08.054
[26] Z. Song, X. Chi, S. Dong, B. Meng, X. Yu, X. Liu, J. Wang, Angewandte Chemie **136**(7), e202317267(2024). https://doi.org/10.1002/anie.202317267
[27] A. Bashir, M. Maqbool, A. Usman, R. Lv, H. Niu, L. Kang, S. Bai, Composites Part A: Applied Science and Manufacturing **173**, 107676(2023). https://doi.org/10.1016/j.compositesa.2023.107676
[28] A. Chaurasia, K. Kumar, S. P. Harsha, A. C. Parashar, Physical Chemistry Chemical Physics **25**(45), 31396(2023). https://doi.org/10.1039/D3CP04321A
[29] N. S. Suhaimin, M. F. R. Hanifah, M. Azhar, J. Jaafar, M. Aziz, A. F. Ismail, R. Mohamud, Materials Chemistry and Physics **278**, 125629(2022). https://doi.org/10.1016/j.matchemphys.2021.125629
[30] D. Losic, F. Farivar, P. L. Yap, T. T. Tung, M. J. Nine, Science of The Total Environment **848**,

157743(2022). https://doi.org/10.1016/j.scitotenv.2022.157743
[31] A. Bouafia, S. E. Laouini, O. B. Ali, H. Daoudi, S. Meneceur, H. A. Mohammed, T. Trzepieciński, Applied Organometallic Chemistry **39**(4), e70119(2025). https://doi.org/10.1002/aoc.70119
[32] R. Zare, H. A. Badehian, Optical and Quantum Electronics **55**(5), 406(2023). https://doi.org/10.1007/s11082-023-04656-6
[33] V. Mututu, A. K. Sunitha, R. Thomas, M. Pandey, B. Manoj, International Journal of Electrochemical Science **14**(4), 3752(2019). https://doi.org/10.20964/2019.04.44
[34] A. Badawi, M. G. Althobaiti, S. S. Alharthi, A. N. Alharbi, A. A. Alkathiri, S. E. E. Alomairy, Applied Physics A **128**(2), 123(2022). https://doi.org/10.1007/s00339-021-05223-8
[35] A. Kirchhoff, T. Deilmann, P. Krüger, M. Rohlfing, Physical Review B **106**(4), 045118(2022).
[36] P. Das, S. Ibrahim, K. Chakraborty, S. Ghosh, T. Pal, Scientific Reports **14**(1), 294(2024).
[37] V. Sahoo, R. N. Bhowmik, S. A. Khan, Materials Chemistry and Physics **296**, 127298(2023).
[38] D. Liu, Y. Wang, Q. Gong, Y. Xia, L. Li, Y. Xue, S. Li, The Chemical Record **24**(7), e202300334(2024).
[39] A. Balapure, J. R. Dutta, R. Ganesan, RSC Applied Interfaces **1**(1), 43(2024).
[40] A. Hayat, M. Sohail, A. El Jery, K. M. Al-Zaydi, S. Raza, H. Ali, M. Z. Ansari, Energy Storage Materials **59**, 102780(2023).
[41] X. Zhang, S. Zhang, Y. Tang, X. Huang, H. Pang, Composites Part B: Engineering **230**, 109532(2022).
[42] L. Upadhyay, S. Dhanapandian, S. Suthakaran, B. Yadav, K. K. Kar, D. Kumar, J. Arikrishnan, Journal of Materials Science: Materials in Electronics **36**(2), 136(2025).
[43] Ö. Budak, Ö. Uğuz, A. Koca, Journal of Energy Storage **47**, 103538(2022).
[44] K. Dhamodharan, A. K. Singh, Journal of Alloys and Compounds **997**, 174732(2024).
[45] D. Krishnamoorthy, A. K. Singh, Energy & Fuels **38**(21), 21468(2024).
[46] M. K. Eswaran, Z. M. Riyas, T. Asaithambi, Journal of Materials Science: Materials in Electronics **36**(14), 1(2025).
[47] Y. Zhao, M. A. Ghanem, G. R. Reddy, S. W. Joo, Ceramics International **50**(24), 55330(2024).
[48] Z. Ji, L. Chen, G. Tang, J. Zhong, A. Yuan, G. Zhu, X. Shen, Small **20**(15), 2306236(2024).
[49] M. Aalim, U. Altaf, A. Rashid, R. Ahmad, A. Sohail, A. Mir, M. A. Shah, Journal of Solid State Electrochemistry **28**(1), 1(2024).
[50] E. Delfani, S. Habibzadeh, M. Pourdayan, L. Naji, M. R. Ganjali, Journal of Materials Chemistry A **12**(10), 5947(2024).
[51] M. Zaman, S. Elaissi, T. R. Aldhafeeri, S. K. Ali, A. Kumar, Ionics (2025). https://doi.org/10.1007/s11581-024-05876-6
[52] M. Girirajan, A. K. Bojarajan, I. N. Pulidindi, K. N. Hui, S. Sangaraju, Coordination Chemistry Reviews **518**, 216080(2024).
[53] C. S. Bongu, M. Arsalan, E. H. Alsharaeh, ACS Omega **9**(13), 15294(2024).
[54] D. Shrestha, Journal of the Korean Wood Science and Technology **50**(4), 219(2022).
[55] Z. M. Riyas, S. Sharmila, P. Priya, M. R. Prabhu, Ionics **31**(5), 4991(2025).
[56] D. Krishnamoorthy, A. K. Singh, Diamond and Related Materials **152**, 111976(2025).
[57] M. Saxena, S. A. Patil, S. Reza, A. Das, R. Thapa, P. K. Misra, ACS Applied Nano Materials **8**(17), 8948(2025).
[58] S. Cui, X. Ren, H. Yin, H. Fan, C. Wang, M. Zhang, Y. Xin, Journal of Energy Storage **85**, 111092(2024).
[59] J. Chen, P. S. Lee, Advanced Energy Materials **11**(6), 2003311(2021).